

LA-UR 96-3487

CONF-9608132--12

Los Alamos National Laboratory is operated by the University of California for the United States Department of Energy under contract W-7405-ENG-36.

RECEIVED

NOV 14 1996

TITLE: RESULTS OF RUSSIAN/US HIGH PERFORMANCE DEMG EXPERIMENT

OSTI

AUTHORS: All Russian Scientific Research Institute of Experimental Physics  
Arzamas-16, Nizhni Novgorod, Russia

A. M. Buyko, N. P. Bidylo, V. K. Chernyshev, V. A. Demidov, S. F. Garanin,  
V. N. Kostyukov, A. A. Kulagin, A. I. Kuzyaev, A. B. Mezhevov, V. N. Mokhov  
E. S. Pavlovskiy, A. A. Petrukhin, V. B. Yakubov, and B. T. Yegorychev

Los Alamos National Laboratory

J. W. Canada (P-22), Carl A. Ekdahl (NWT-PO), James H. Goforth (DX-3),  
James C. King (DX-4), Irvin R. Lindemuth (X-PA),  
Robert E. Reinovsky (DX-DO), Patrick. Rodriguez (P-22), R. C. Smith (P-22),  
Lynn R. Veaser (P-22), and Stephen M. Younger (NWT-PO)

SUBMITTED TO: The Seventh International Conference on Megagauss Magnetic Field  
Generation and Related Topics; August 5-10, 1996;  
Sarov (Arzamas-16), Russia

By acceptance of this article, the publisher recognizes that the U.S. Government retains a nonexclusive, royalty-free license to publish or reproduce the published form of this contribution, or to allow others to do so, for U.S. Government purposes.

The Los Alamos National Laboratory requests that the publisher identify this article as work performed under the auspices of the U.S. Department of Energy.

DISTRIBUTION OF THIS DOCUMENT IS UNLIMITED

Los Alamos

Los Alamos National Laboratory  
Los Alamos, New Mexico 87545

MASTER

**DISCLAIMER**

**Portions of this document may be illegible in electronic image products. Images are produced from the best available original document.**

## DISCLAIMER

This report was prepared as an account of work sponsored by an agency of the United States Government. Neither the United States Government nor any agency thereof, nor any of their employees, makes any warranty, express or implied, or assumes any legal liability or responsibility for the accuracy, completeness, or usefulness of any information, apparatus, product, or process disclosed, or represents that its use would not infringe privately owned rights. Reference herein to any specific commercial product, process, or service by trade name, trademark, manufacturer, or otherwise does not necessarily constitute or imply its endorsement, recommendation, or favoring by the United States Government or any agency thereof. The views and opinions of authors expressed herein do not necessarily state or reflect those of the United States Government or any agency thereof.

**RESULTS OF RUSSIAN/US HIGH PERFORMANCE DEMG EXPERIMENT<sup>1</sup>**

A. M. Buyko, N. P. Bidylo, V. K. Chernyshev, V. A. Demidov, S. F. Garanin,  
V. N. Kostyukov, A. A. Kulagin, A. I. Kuzyaev, A. B. Mezhevov, V. N. Mokhov,  
E. S. Pavlovskiy, A. A. Petrukhin, V. B. Yakubov, B. T. Yegorychev

All Russian Scientific Research Institute of Experimental Physics  
Arzamas-16, Nizhni Novgorod, Russia

J. W. Canada, C. A. Ekdahl, J. H. Goforth, J. C. King, I. R. Lindemuth,  
R. E. Reinovsky, P. Rodriguez, R. C. Smith, L. R. Veaser, S. M. Younger

Los Alamos National Laboratory  
Los Alamos New Mexico, USA

**ABSTRACT**

In November 1992, the All Russian Scientific Research Institute of Experimental Physics (VNIIEF), Arzamas-16, Russia and the Los Alamos National Laboratory, Los Alamos NM, USA embarked on a historic effort to conduct a joint explosive pulse-power experiment. With the concurrence of the Ministry of Atomic Energy (Russia) and the Department of Energy (USA), the two laboratories, entered into a Laboratory-to-Laboratory collaboration in the areas of very high energy pulse-power and ultrahigh magnetic fields in order to explore problems of mutual scientific interest. The first experiment to be planned was an explosively powered, fast, high-current pulse-power system demonstration. The experiment used a flux compressor, inductive store, and high-current opening switch to demonstrate the feasibility of supplying many megajoules of electrical energy, on microsecond time scales, to high energy density physics experiments. The experiment was conducted in Arzamas-16 on September 22, 1993.

---

<sup>1</sup>This work supported by the Department of Energy.

## I. SYSTEM DESCRIPTION

The key element in the experiment was a Russian-designed, very high current, fast, flux compressor based on the Disk Electromagnetic Generator (DEMG) geometry. The major components of the system are outlined in Fig. 1 and included a capacitor bank (not shown), a helical flux explosive compressor, a disk explosive flux compressor, a fast electro-explosive (fuse) opening switch, an explosively operated solid dielectric load isolating closing switch, and an imploding aluminum liner.

The performance of a system combining a DEMG and fuse opening switch had previously been reported.<sup>2</sup> The joint experiment was designed to extend that demonstration to a system including a dynamic load. Initial flux, about 2.9 webers, was provided from the capacitor bank to the helical preamplifier through an inductive coupling coil. The output of the helical preamplifier, about 6.6 MA, was directly connected to the DEMG. A crowbar switch, designed to trap flux in the disk stage after helical operation, was included between helical and disk stages. The output current from the DEMG, peaking at about 50 MA, was carried by a cylindrical copper foil fuse located immediately outside the disk stages. The liner load was connected across the fuse through a low inductance, coaxial, solid dielectric transmission line. The load was isolated from the DEMG circuit by a series, explosively operated, solid dielectric closing switch. Current measurements were made by B-dot probes arranged in rings at several stations along the system. B-dot measurements were correlated with electro-optic magnetic field measurements made by Faraday rotation at two of the stations. The imploding liner, initially 3 cm in radius and 2-cm tall moved several millimeters before being vaporized by the load current that reached 20 MA in less than 1  $\mu$ s. The implosion reached final velocities of about 3.1 cm/ $\mu$ s. Measurements of load behavior included B-dot, and fiber optical and electrical contact pins.

## II. DESIGN CALCULATIONS

### A. Calculational Model

Using computational techniques, that have previously been benchmarked against test results reported in the literature,<sup>3,4</sup> performance of the Joint Experiment was calculated. Performance of the helical generator has been confirmed in numerous tests and, for modeling purposes, was characterized as a range of initial currents delivered to the DEMG. The DEMG model calculates motion of the disk generator cavity walls using a modified instantaneous acceleration (Gurney<sup>5</sup>) model, and magnetic pressure in the cavity. Diffusion of magnetic field is calculated into the walls of the disk generator and into the transmission line associated with each disk stage. Magnetic diffusion into the walls of the transmission line leading to the liner load is not calculated. The operation of the fuse opening switch is calculated using the "CONFUSE" model as previously reported.<sup>6</sup> The CONFUSE code models the fuse as a uniform ohmically heated metal layer whose expansion in one dimension is limited by moving but uniform nonconducting walls. The closing switch model approximates a multichannel switch with each channel having a characteristic resistivity. Multiple channels are added in parallel with a fixed time interval between channels. The liner load is modeled as a "zero-dimensional," right-circular cylinder. Current in the liner cross section is considered constant (the field is fully diffused) from the beginning of acceleration. Specific energy (joule/gram) is calculated in the liner material and the resistance of the liner is calculated from tabular resistivity vs. energy data. The generator, fuse, closing switch, and liner behavior is expressed as equivalent circuit elements (resistances and inductances) and the circuit elements are connected in a simple, two-loop network calculation to determine generator and load currents. In this way, load behavior is coupled to generator performance through generator loop current (and its effect on generator wall motion).

## B. Parameters for the Experiment

For the Joint Experiment, we calculate the behavior of a 15-module Disk Explosive Magnetic Generator (DEMG) using an approximate cavity profile and a 2-mm copper wall. The dimensions of the DEMG (half) cavity are shown in Fig. 2.

The inductance of the cavity and transmission line to the initial radius of the fuse was specified to be 11.6 nH, and the system inductance from crowbar (which isolates the DEMG from the helical preamplifier) to fuse was 178 nH. The system inductance consists of 175.5 nH in the generator cavities and transmission lines, 1.82 nH in the crowbar switch, and 0.55 nH of additional inductance in the diagnostic stations. An initial current of 6.0 MA was assumed. For modeling purposes, an explosive composed at 70% RDX and 30% TNT was used. The detonation velocity of the mixture was taken to be 8.17 cm/ $\mu$ s. The density was 1.78 g/cm<sup>3</sup>. The gurney energy is 2.78 and the detonation pressure about 310 kbar. The total mass of explosives in the DEMG was about 105 kg.

To generally characterize a 15-module generator, we calculate the estimated performance of system when operated into a 3.7-nH inductance representing approximately the inductance of the system transmission line up to the fuse, the crowbar switch, and the diagnostic system. Under these circumstances, the generator would be expected to produce 55 MJ of electrical energy at about 170 MA. The current and energy for this characterization case is shown in Fig. 3. With a fuse in the circuit the peak generator current is limited about 60 MA.

Calculations were performed using a 155-mm copper foil fuse 1.08-m long and 1.315-m wide. The CONFUSE model predicts behavior for the fuse ranging from complete interruption (and high final resistivity) to reconnection (with relatively low final resistivity). For these calculations, a resistivity model that includes a sharp resistivity increase and good current interruption was chosen because, as will be seen in the wave forms, the sharp rise in resistivity produces substantial stress in the transmission line insulation. However, a ceiling value is imposed on the fuse resistivity corresponding to a maximum fuse resistance of about 21 m-ohms. The transmission line inductance between the fuse and the initial position of the liner load was

8.55 nH. In the calculations, the beginning (first channel closure) of current conduction in the load isolation switch was specified to occur at 19.9  $\mu$ s. The individual channel resistivity is 10 m $\Omega$ , and the interchannel time is 300 ns. The closing switch was supporting about 73 KV at the time that closure was initiated.

The liner load was 3 cm in radius and 2-cm high, with a design thickness of 0.3 mm. The specific energy in the liner resulting from ohmic heating was calculated during implosion and the resistance rise due to liner heating was included in the calculation. The liner vaporized at about 21.45 ms, 1.55 ms after beginning of current flow in the load. At the time of liner vaporization, the outer radius of the liner had moved 3.2 mm or about 11 times its initial thickness. The diagnostic package was located at a radius of 4.5 mm. The inner surface of the liner reaches the diagnostic package 2.35 ms after the beginning of current in load. At this time the liner had undergone a radial compression of about 6, reached a peak velocity of about 4.2 cm/ms and a kinetic energy of 3.2 MJ.

### C. Projected Performance

The purpose of the point design was to identify the relationship between various aspects of the system's operation and to provide a quantitative basis for selection of diagnostic parameters. Figure 4 shows the performance of the DEMG expressed as the time-varying inductance and the time-varying resistance. The inductance of the fifteen generator cavities was initially 174 nH and decreased to approximately 4 nH at 23  $\mu$ s. These calculations, we begin with no magnetic field in the conductor. In other words, we assume that the flux due to the initial current was limited to the cavity gap. Thus, early in the calculation, before the walls of the cavities move, flux is diffusing rapidly into the walls, and this leads to a significant early time resistance of several milliohms. In the experiment, the helical generator introduces flux into the generator over several hundred microseconds and the flux is probably full diffused into the walls of the DEMG. Therefore, this calculation overestimates the loss due to diffusion in early time.



Calculated current in the generator and load loops are shown in Fig. 5. Initial current in the calculation was 6 MA (midway between the 5.5 and 6.5 MA expected from the helical generator). Peak generator current of about 61 MA occurs at about 20.5  $\mu\text{s}$ . (about 600 ns after the beginning of the closure of the isolation switch). Peak calculated current in the load was approximately 36 MA at about 21.7  $\mu\text{s}$ . The fuse current was calculated from the difference between generator and load currents. The fuse current shows a small increase at about 22.1  $\mu\text{s}$  as the inductance of the imploding liner rises.

Figure 6 shows the time derivative of the generator, fuse and load current calculated for the full experiment but displayed on expanded time scale. Several distinct features can be observed in the calculated  $dI/dt$  histories, including the opening of the fuse opening switch, the closing of the load isolation switch, and the implosion of the liner load. Figure 6a shows the generator current derivative and includes calculated histories (dotted lines) showing  $dI/dt$  for the case where the fuse interrupts the current, and the closing switch fails to close. The figure also shows the behavior of the generator  $dI/dt$  for the case where current is switched into the load loop, but the liner does not implode.

Figure 6b shows the calculated time derivative of the current in the fuse. Several features of the system's operation can be seen including the time of closure of the load isolation switch and the implosion of the liner. The fuse resistance profile used in the calculations include a sharp rise in resistance upon fuse vaporization and this feature is identifiable in the fuse  $dI/dt$  at 21.25  $\mu\text{s}$ . Similarly, the explosion of the liner due to ohmic heating is seen at 21.45  $\mu\text{s}$  and the time of maximum liner compression (impact on the diagnostic package) is identifiable at 22.25  $\mu\text{s}$ . The calculated fuse current peaks at about 60 MA and decreases as current is transferred to the load loop. Figure 6c shows the time derivative of the current in the liner load. The same features identified in the fuse  $dI/dt$  can be identified in the load  $dI/dt$ . The peak load current is slightly over 36 MA.

Figure 7 shows the resistance calculated for the fuse and the voltage along the fuse as a function of time. The sharp rise in fuse resistance is terminated at 21 m $\Omega$  based on VNIIEF

experience. The features already identified in the  $dI/dt$  signals are also present in the fuse voltage. The sharp rise in fuse resistivity leads to a peak in fuse voltage approaching 500 KV, which can overestimate the voltage observed in the experiment depending on the precise behavior of the fuse resistivity. The earlier maximum in the fuse voltage (418 KV at 20.85  $\mu$ s) is responsible for driving the majority of the current into the load. Upon compression, the time changing inductance of the liner gives rise to an increase in fuse voltage at 22.25  $\mu$ s.

Figure 8 shows the radius of the liner during the implosion process and the liner kinetic energy, which reaches about 3.2 MJ at the time of impact on the diagnostic package. The liner velocity reaches about 4.2 cm/ $\mu$ s. While the model calculates the ohmic heating of the liner and should correctly identify the time of vaporization (explosion), it does not calculate liner expansion or recompression after vaporization. Thus, the model assumes that the liner maintains constant density through the entire process and this explains why the inner and outer radii shown in Fig. 11 do not show substantial expansion after liner vaporization.

### III. CAPACITOR BANK AND HELICAL FLUX COMPRESSOR OPERATION

The DEMG main energy amplifier required 1.2 webers of magnetic flux at about 6.5 MA. A helical flux compressor from the VNIIEF family of POTOK generators was used to provide the initial flux to the 15-element DEMG. The helical generator consisted of a wire-wound stator coil with an inner diameter of 240 mm and a length of 1200 mm. The initial inductance of the stator coil is 48 nH. The armature of the generator consists of a copper central tube filled with a 21-kg charge of high explosive whose composition was 70% RDX and 30% TNT.

Initial flux is introduced into the helical flux compressor through a 28-turn coupling coil wound over the outside of the helical stator at a diameter of 280 mm and covered with epoxy. The length of the coil was 1000 mm and the coupling coefficient was 75%. Since the coupling is significantly less than 100%, this technique introduces some inefficiency in the initial loading process but offers several advantages. First, by allowing the helical/DEMG/fuse circuit to be open prior to the operation of the helical generator, the inductive loading insures that the fuse

carries no current, and hence is at room temperature when the system begins to operate. Second, the inductive coupling allows the ground connection of the capacitor bank system to be completely separate from the flux compressor ground circuit. This allows for easy isolation of the flux compressor system diagnostics from ground.

With the 1200- $\mu$ F capacitor bank charged to 24 kV, the current in a coupling coil was 79.3 kA. Initial flux in a preamplifier is equal to 2.9 Wb (which was close to the planned value of 3.0 Wb). In order to prevent the flux compressor from driving substantial current and energy back into the capacitor bank circuit, the initial loading circuit is interrupted with a simple, explosively operated, opening switch.

Figure 9 shows the current derivative and the current in the preamplifier circuit obtained from the average of all measuring probes located at the C-ring.

The design value of the preamplifier output current was 6.0 MA. In the experiment, average peak current from all the probes in the helical stage was 6.6 MA. The maximum value of the current derivative averaged from all the C-ring probes in the preamplifier was  $2.1 \times 10^{11}$  A/sec, and the characteristic e-fold rise time of current is 28  $\mu$ s. These results demonstrate that the performance of the helical flux compressors was essentially as projected.

#### IV. PERFORMANCE OF THE DISK EXPLOSIVE MAGNETIC GENERATOR

The operation of the DEMG was recorded by probes in the  $\Delta$ -ring, located as shown in Fig. 1. All data is timed relative to the operation of the detonator firing unit. The beginning of measurable current derivative in the DEMG occurs in a range from  $t = 5$  to  $t = 6$   $\mu$ s. It should be noted that the observed beginning of measurable I-dot takes place somewhat after the first motion of the metallic walls in the magnetic flux compression cavities. Onset of measurable I-dot depends on the rate of magnetic flux diffusion losses in the walls, on crowbar dynamic resistance, and on differences in time of HE initiation in disk elements.

Figure 10a shows the current derivative in the DEMG as recorded by the  $\Delta$ -ring probes (over the time interval  $t = 0$  to  $t = 35$   $\mu$ s. After reaching a maximum, corresponding to the time

near the end of the DEMG operation when the fuse opening switch begins to rise significantly in impedance, the current derivative is seen to decrease rapidly and become negative as the fuse opening switch rises rapidly in impedance. After the brief negative excursion,  $I\dot{\phantom{I}}$  again rises to approximately its former value. Records from a total of five probes in the "Δ"-ring are plotted in Fig. 10a. The maximum value of a current derivative at the first positive peak for all five probes is in the range from  $0.82$  to  $1.00 \times 10^{13}$  A/sec. At the negative peak the amplitude for all five probes is in the range from  $0.22$  to  $0.37 \times 10^{13}$  A/sec, and the second positive peak amplitude is from  $0.9$  to  $1.00 \times 10^{13}$  A/s. Averaging the five probes results in amplitude of the current derivative of  $0.9 \times 10^{13}$  A/s at the first positive peak (associated with the end of generator operation at  $t = 25.2 \mu\text{s}$ ). The average for the negative peak associated with the operation of the fuse is  $0.31 \times 10^{13}$  A/s at  $t = 26.23 \mu\text{s}$  and of the second positive peak was  $0.97 \times 10^{13}$  A/s.

Figure 10b shows time dependence of DEMG current found from integrating the averaged current derivative. Current value at the moment of the first peak (near the end of DEMG operation) was  $48.2$  MA (at  $t = 26.0 \mu\text{s}$ ). The current then decreases to about  $47.4$  MA (at  $t = 26.45 \mu\text{s}$ ). The current in the DEMG then increases to almost to  $70$  MA.

## V. CURRENT DELIVERY TO THE LOAD

To measure current delivery to the load, inductive probes were located in probe rings at two positions downstream of the fuse as shown in Fig. 1. One of the probe rings was located at the beginning of a coaxial transmission line ( $\Pi$  probes) and the other ring was located at the input of a radial transmission line—the output end of the coaxial transmission line—( $\Phi$  probes). Six  $\Phi$  and six  $\Pi$  probes (twelve in all) were used in the experiment.

Figure 11 compares signals from  $\Delta$ ,  $\Pi$ , and  $\Phi$  probes. Inspection of the plots shows that pulse shapes, recorded by  $\Pi$  and  $\Phi$  probes differ in significant ways. Both the  $\Pi$  and  $\Phi$  probe records contain readily identifiable jumps in current derivative at about  $26 \mu\text{s}$  and the discontinuities are in different directions. The records from  $\Pi$  probes have the jumps with a signal increase, and the records from  $\Phi$  probes show a signal decrease. Furthermore, the signal

from  $\Pi$  probes is substantially wider when compared to the width of the  $\Phi$  probes. And signals from  $\Pi$  probes show positive values for all times of interest (indicating constantly increasing current) while signals from the  $\Phi$  probes have a portion with a negative component of the current derivative (indicating a decreasing current). Taken together the P-ring and  $\Phi$ -ring data argue strongly for a partial failure of the transmission line insulation at a location between the two rings during the time when current was being transferred to the liner load.

The current in the DEMG ( $\Delta$ ) and at the  $\Pi$  and  $\Phi$  locations is calculated from the integral of the current derivatives and are shown in Fig. 12. This plot gives averaged current curves for all  $\Pi$  probes and all  $\Phi$  probes. It is seen from the plot that current in the load before  $26 \mu\text{s}$  (the time of the first jump on a current derivative) recorded by both  $\Pi$  and  $\Phi$  probes match. After  $26 \mu\text{s}$  the two probes disagree sharply. Maximum current value in the place where  $\Pi$  probes have been located (i.e., at the input of a coaxial transmission line), comes close to the current value in the DEMG. The current histories support the conclusion that some current was shunted between the  $\Pi$  and  $\Phi$  locations.

Simple circuit analysis can be applied to estimate the location of the partial breakdown in the transmission line. At the time of the breakdown  $dI/dt$  measured at either  $\Pi$  and  $\Phi$  locations is about  $3.0 \times 10^{13} \text{ A/s}$  and the inductance downstream of the fuse is  $8.55 \text{ nH}$ . These values lead to the conclusion that the fuse voltage at the time of the failure was about  $255 \text{ KV}$ .

Figure 11 shows an approximate average value of the positive jump in current derivative at the  $\Pi$ -ring is  $1.4 \times 10^{13} \text{ A/sec}$  and the average value of the negative jump from the  $\Phi$ -ring is about  $-0.8 \times 10^{13} \text{ A/sec}$ . Treating the partial failure as an inductance shunting the line, we find that the point of the partial transmission line failure was about  $3.2\text{-nH}$  downstream from the fuse or about  $5.3\text{-nH}$  upstream from the load and that the value of the shunt inductor is about  $5.3 \text{ nH}$ . Immediately before the failure, inductive division in the transmission line lead to the conclusion that the voltage at the point of the failure was about  $160 \text{ KV}$ . Immediately after the failure, the voltage at the failure point dropped to about  $115 \text{ KV}$ .

## VI. OPERATION OF THE LINER IMPLOSION (PONDERMOTIVE UNIT)

The imploding liner consists of an aluminum cylinder 3 cm in radius, 2-cm high, and 0.03-cm thick. The total mass of the imploding load is 3.05 gr. Inside the liner, a cylindrical diagnostic package is located at a radius of 4.75 mm. The package includes inductive, electrocontact and light probes and is surrounded by a thin tantalum cylinder that protects the probes from impact of low density plasma thrown ahead from the vaporization of the liner. The tantalum shell is connected to the electrodes providing a current path that allows some flux to leak through the finite resistance of the main liner and is thin enough to be swept up by the massive liner as it implodes.

Inductive probes located inside the initial radius of the liner were used to record the time derivative of magnetic field appearing inside the liner. For this purpose, four inductive probes were imbedded in the glide planes along which the liner moves at a radius of 9 mm. A dielectric cylinder insulates the slot leading to the buried probes and ensures that the probes are sampling the interior field until the liner sweeps over the feed slot. The time history of the magnetic field inside the liner interpreted as a current derivative is presented in Fig. 13. Four peaks are observed in the current derivative inside the liner. The time of the first maximum, from the average of four individual probes, is 26.53  $\mu\text{s}$ , which corresponds to 1.29  $\mu\text{s}$  from the beginning of current flow in the liner. The first maximum value is in the range from 2.2 to 3 MA/sec. Three more peaks are observed in the current derivative. The averaged times for these maximum values are 27.60 sec (the second maximum), 27.97 sec (the third maximum), and 28.36 sec (the fourth maximum), correspondingly. The time of each maximum is simultaneous on each probe to within 100 ns.

The first maximum is associated with the electric explosion (vaporization) of the liner. The calculation presented in Fig. 6c shows the liner exploding about 1.3  $\mu\text{s}$  after onset of current in the load—in good agreement with the measurement in Fig. 13. The second peak is associated with the compression of magnetic field inside the liner. (The flux being compressed enters the

space inside the liner during the electro-explosion of the liner and is supported by current flowing in the tantalum shell surrounding the diagnostic package.)

At the third peak, approximately  $2.77 \mu\text{s}$  after onset of current in the load, the probe is measuring the magnetic field outside the liner after it passes the probe. In fact the field outside the liner is substantially greater than what would be inferred from the value of the third peak in Fig. 13. As the liner passes the insulated slot leading to the probe, a thin layer of conductive material is expected to be left behind, partially shielding the probe from the driving field. From the trajectory plotted in Fig. 8, we would expect the liner to arrive at the radius of 9 mm about  $2.1 \mu\text{s}$  from the onset of current. The delayed arrival is consistent with the lower driving current resulting from the partial shunting of the transmission line discussed above. The fourth peak is associated with the turn-around of the liner outer surface after collision with tantalum shell and the recompression of the field outside the liner resulting from the expanding of the liner.

Electrocontact probes in the central diagnostic package recorded the symmetry of liner flight by measuring the time of arrival of the liner at the measuring unit. A total of 30 probes were employed, arranged in 6 vertical columns of 5 probes each and were located at the radius of 4.75 mm. Data from the probes consist of time of arrival recorded digitally on an array of time interval meters. Figure 14 shows closure times of electrocontact probes plotted as a function of axial position ( $z$ ) and azimuthal location ( $\phi$ ). Time is measured from the moment of the common system trigger. The earliest time of arrival of the liner at the measuring unit was  $27.876 \mu\text{s}$  ( $z = 1 \text{ mm}$ ,  $\phi = 300$ ), the latest time of arrival was  $28.274 \mu\text{s}$  ( $z = 19 \text{ mm}$ ,  $\phi = 0$ ). Maximum difference in time of probes closure (over both axial and radial coordinates) was  $0.398 \mu\text{s}$ . The precision of pulse recording by the time interval meters is  $0.5 \text{ ns}$ , making nanosecond precision in the arrival times justified.

Figure 14a shows that arrival at the measuring unit, the liner had a conic shape. The part of the liner that arrived soonest was near the upstream electrode. Because the liner was assembled to the experiment from the downstream side shortly before the experiment, special attention was paid to the current contact to the upstream end of the liner. The contact between

the liner and the upstream electrode was made by thermal expansion of a brass ring, initially cooled to liquid nitrogen temperature. Upon warming, the ring expanded and clamped the upstream end of the liner assembly to the electrode. While making a good contact, the expanding ring also compressed the soft aluminum liner, perhaps thinning it in the process. Since the liner deforms plastically for a few hundred nanoseconds before vaporizing, differences in mechanical connection on the two ends could have allowed the upstream end to shear and break free at an earlier time, thus allowing it to implode ahead of the downstream end.

In Fig. 15, we plot current derivative at three locations; the  $\Pi$  and  $\Phi$  locations from Fig. 11 and the current derivative inside the liner "A" from Fig. 13. The figure shows that the current derivative in the  $\Phi$  probes is initially positive as current is delivered to the liner, then becomes negative as the liner implodes (with almost constant flux in the inductance outside the liner because of the breakdown in the coaxial line). Later, the current derivative suddenly jumps from negative to positive again. The time of current derivative transition through zero, according to four out of five "F" probes is from 28.2 to 28.4  $\mu\text{s}$ . From Fig. 13 the fourth peak in the "A" probe occurs at 28.3  $\mu\text{s}$ . From Fig. 14, the time of arrival of the liner at the electrocontact probe is from 27.9 to 28.3  $\mu\text{s}$ . Taken together, this suggests that the transition from negative to positive is associated with the turnaround of the outer edge of the liner after it collides with the measuring unit and begins to recompress a magnetic flux outside the liner.

## VII. RESULTS

In Sec. 3, we presented preshot predictions of the performance of the experiment. The preshot calculations did not include the effect of the partial transmission line failure. Using the analysis in Sec. 6, we determined the approximate location of the transmission line failure. Modeling the failure as an inductive shunt applied across the line at the appropriate time, the current derivative in Fig. 16 were obtained. A time shift was applied to roughly align the maximum negative excursion in current derivative resulting from the fuse opening. Good agreement was noted between the model and the experiment at the peak value of the generator



current derivative before the fuse operation; at the peak negative excursion during fuse operation (and subsequent closing of the load isolating switch) and at the first peak positive value of the current derivative after the closure of the crowbar switch. Some significant differences are noted in the current derivative at times prior to the first peak, and these were attributed to differences between the assumed and actual profile of the DEMG cavities. Significant differences are also noted at late times—well after the formation of the transmission line short. The discontinuity analysis in Sec. 6 applies immediately after the shunt is applied and assumes a lossless, inductive shunt. The late time differences between model and experiment in Fig. 16 can be attributed to a substantial change in shunt impedance with time as large currents flow through the shunt.

After the system was completely assembled, it was possible to accurately measure all relevant dimensions, and a more accurate "as built" characterization of the fuse, transmission line, diagnostic cavities, radial feed, and load were found. When these adjustments are made and the system performance recalculated, the results are shown in Fig. 17. In the figure, the measured generator current derivative from the  $\Delta$ -ring and the calculated derivative are shown to correspond closely. Not only do the timing and magnitude of the maximum (prior to fuse operation) correspond accurately, but relatively small features during the generator operation prior to peak  $di/dt$  correspond as well. For example, the small feature in the calculation around  $16 \mu\text{s}$  (resulting from the arrival on the symmetry plane of one of the corners in the generator cavity) is seen to correspond to a similar (though less distinct) feature in the experiment. In the experiment, small differences in timing and performance between cavities could be expected to lead to substantial smoothing of the current derivative.

With the results in Fig. 17, we can have reasonable confidence in the adequacy of current DEMG models to provide reasonable prediction of system behavior. Systems using fuse opening switches and dynamic loads can likewise be adequately modeled.

## VIII. REFERENCES

1. V. K. Chrenyshev, M. S. Protasov, and B. A. Shevtsov, "The First Disk Explosive Generators," in *Proceedings of the 3rd International Conference on Megagauss Fields and Applications*, Novosibirsk, Russia (1983).
2. V. K. Chernyshev, A. M. Boyko, V. N. Kolstyukov, A. I. Kuzyaev, A. A. Kulagin, V. I. Mamyshev, A. B. Mezhevov, A. I. Nechaev, A. A. Petrukhin, M. S. Protasov, V. I. Shvetsov, and V. B. Yakubov, "Investigation of Electrically Exploded Large Area Foil for Current Switching," *Megagauss Fields and Pulsed Power System*, Nova (1990) p. 465.
3. R. E. Reinovsky, I. R. Lindemuth, S. P. Marsh, and E. A. Lopez, "Explosive Pulse Power for Fusion Applications," in *Proceedings of 6th International Conference on Megagauss Fields and Applications*, Albuquerque, NM (1992).
4. R. E. Reinovsky and I. R. Lindemuth, "Design Considerations for 100 MJ Class Flux Compression Pulse Power Systems," in *Proceedings of the 9th IEEE International Pulsed Power Conference*, Albuquerque, NM (1993).
5. J. E. Kennedy, "Gurney Energy of Explosives: Estimation of the Velocity and Impulse Imparted to Driven Metal," Sandia National Laboratory, SC-RR-70-790.
6. I. R. Lindemuth, R. E. Reinovsky, and J. H. Goforth, "Exploding Metallic Fail Fuse Modeling at Los Alamos," *Megagauss Fields and Pulsed Power System*, NOVA, p. 269 (1990).

## Figure Captions

Fig. 1. Schematic view the Joint DEMG experiment.

Fig. 2. Approximate profile of the (half) cavity of the DEMG.

Fig. 3. The DEMG is capable of very large energies when operated into a low inductance (3.74-nH) load.

Fig. 4. The DEMG system is 15 modules using a configuration virtually identical to that of the previous experiments.

Fig. 5. Peak generator currents was calculated to be 60–61 MA. Peak load current was calculated to be almost 36 MA.

Fig. 6 (a,b,c). The main features of the experiment are identifiable in the current derivatives.

Fig. 7. The CONFUSE resistance is limited to 20 m $\Omega$  and the fuse produces almost 500 kV. The closing switch supports 75 kV at closing time.

Fig. 8. The liner reaches the radius of the diagnostic package in 2.35  $\mu$ s, reaching a velocity of 4.2 cm/ $\mu$ s.

Fig. 9.  $dI/dt$  and current in the helical generator. Plots are an average of five probes located in the C-ring (shown in Fig. 1).

Figure 10. (a)  $dI/dt$  in DEMG and (b) Current in the DEMG.

Figure 11. Comparison of  $dI/dt$  in DEMG ( $\Delta$ ) with that immediately downstream of the fuse ( $\Pi$ ), and that further down the transmission line near the load ( $\Phi$ ).

Figure 12. Current in DEMG ( $\Delta$ ), current immediately downstream of the fuse ( $\Pi$ ), and current in the transmission line near the load ( $\Phi$ ).

Figure 13. Magnetic field inside the liner recorded on probes located at radius of 9 mm, expressed as  $dI/dt$ .

Figure 14. (a) Time of arrival as a function of axial position indicated by contact pins in the central measuring unit. Liner connect probes at the same azimuth (b) time of arrival as a function of azimuth indicated by contact probes, line connect probes at the same z.

Figure 15. Comparison of  $dI/dt$  inside and outside the initial position of the liner.

Figure 16. Comparison of the  $\Delta$ -ring current derivative with a calculation using the model discussed in Sec. 3 with the addition of a transmission line shunt.

Figure 17. Current derivative from the experiment and the calculation corrected for "as-built" dimensions.

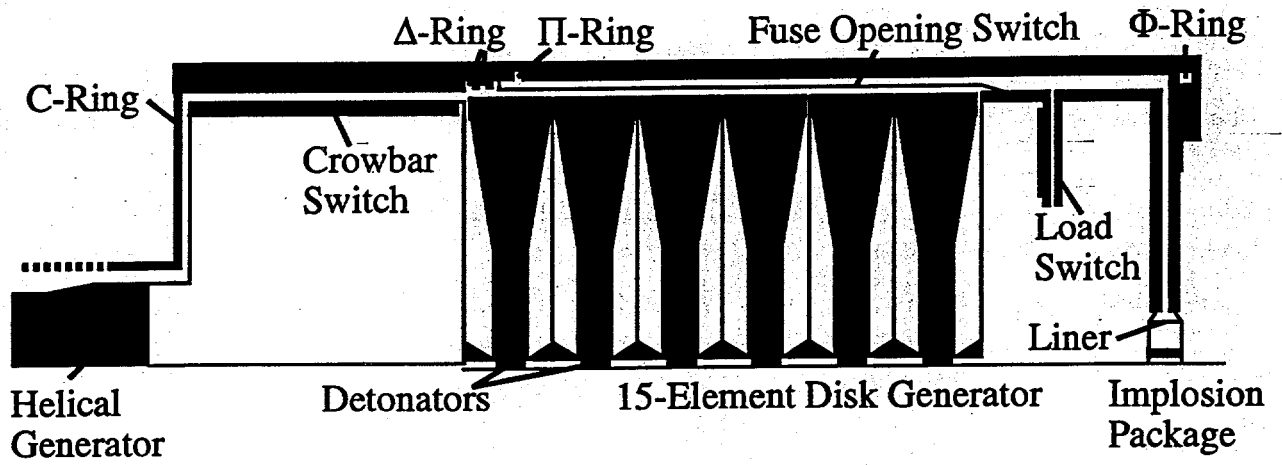


Figure 1.

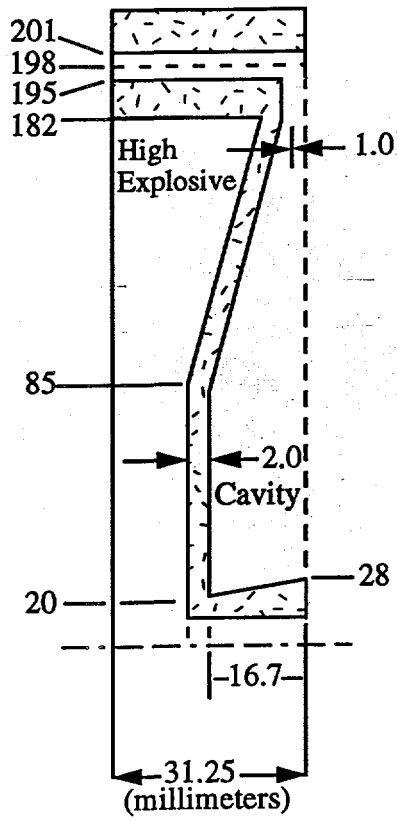


Figure 2.

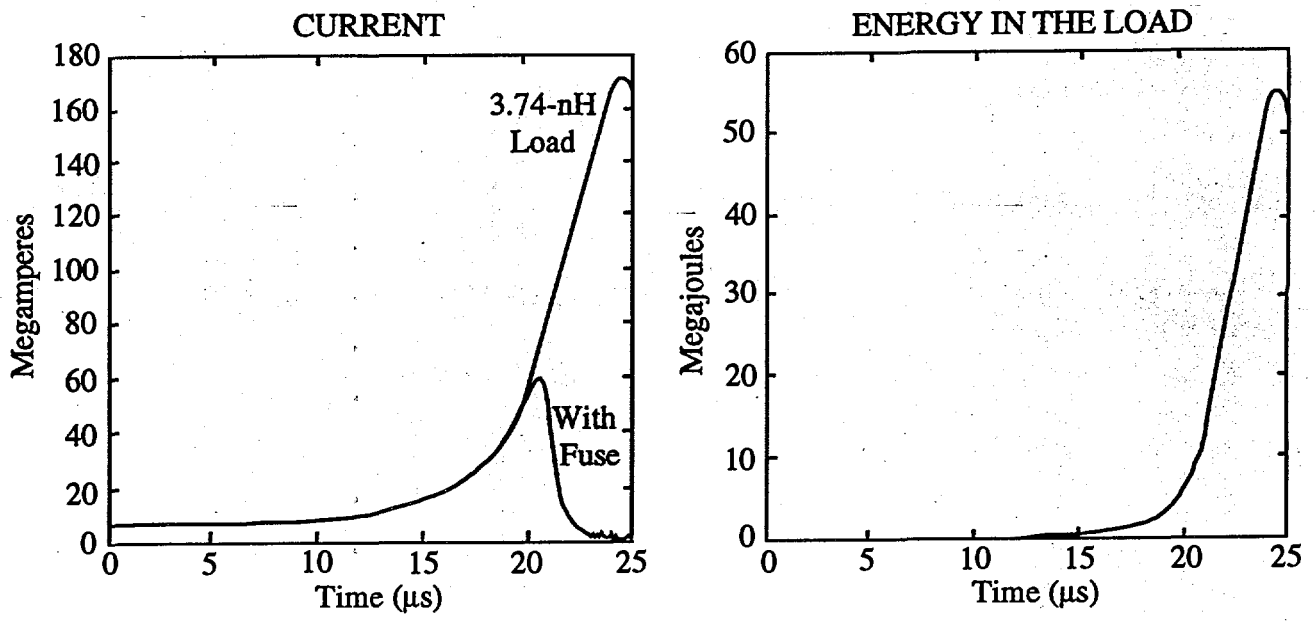


Figure 3.

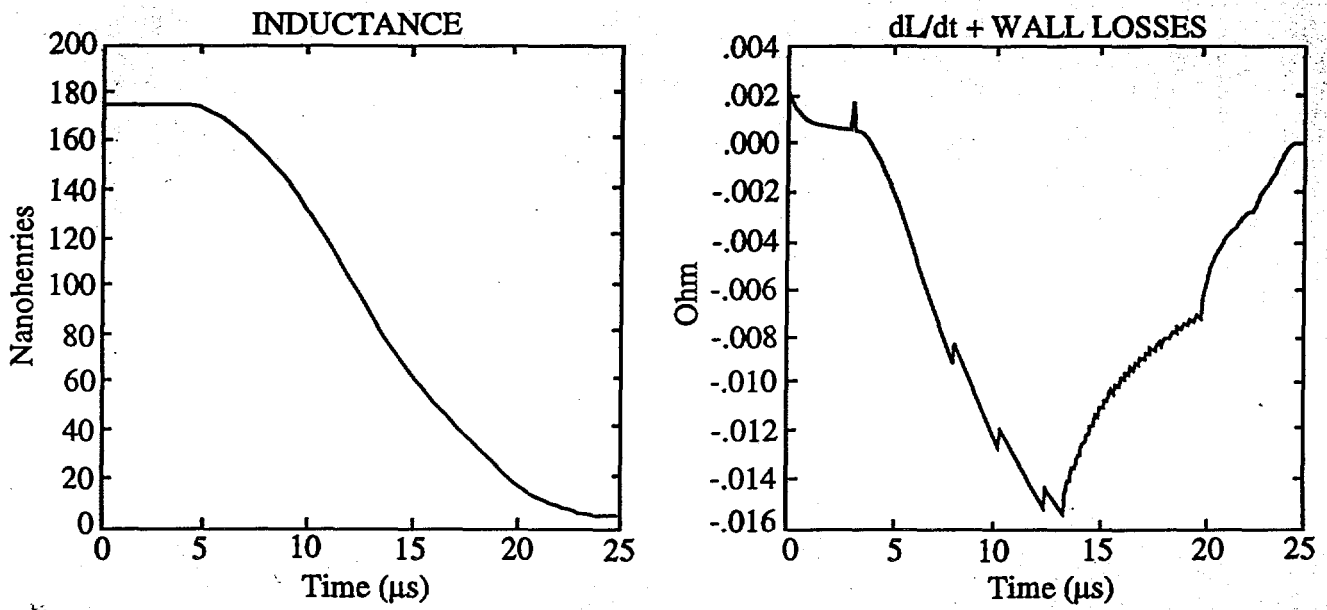


Figure 4.



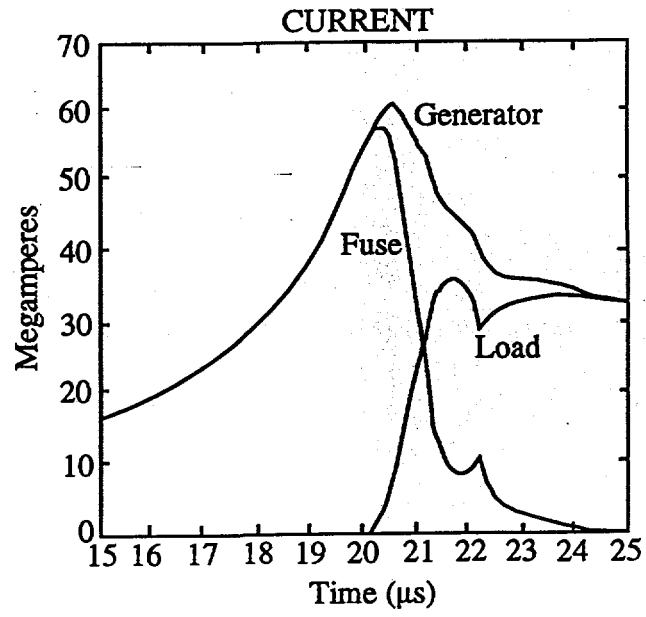


Figure 5.

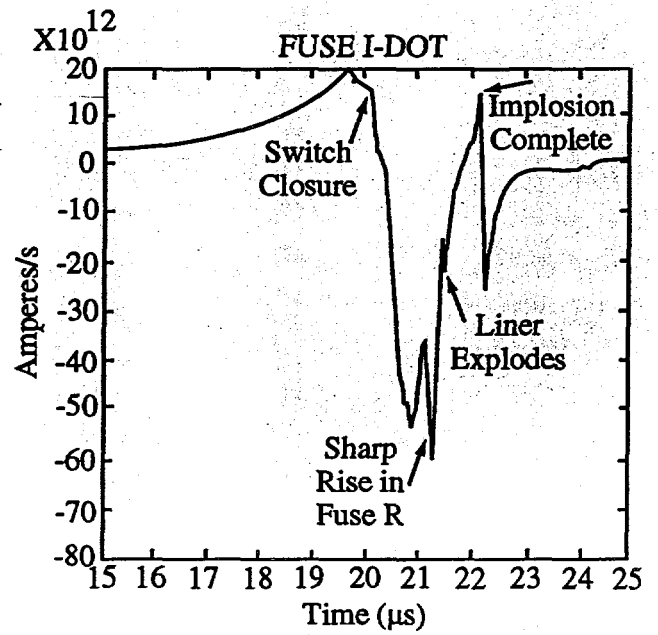
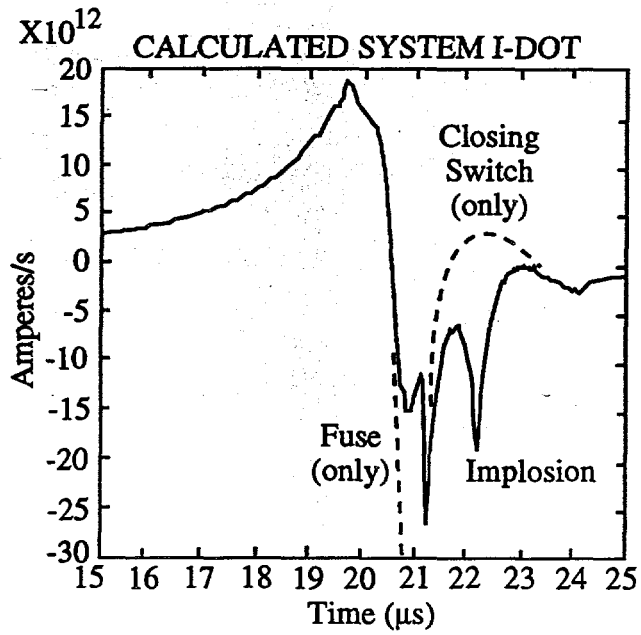


Figure 6a and b.

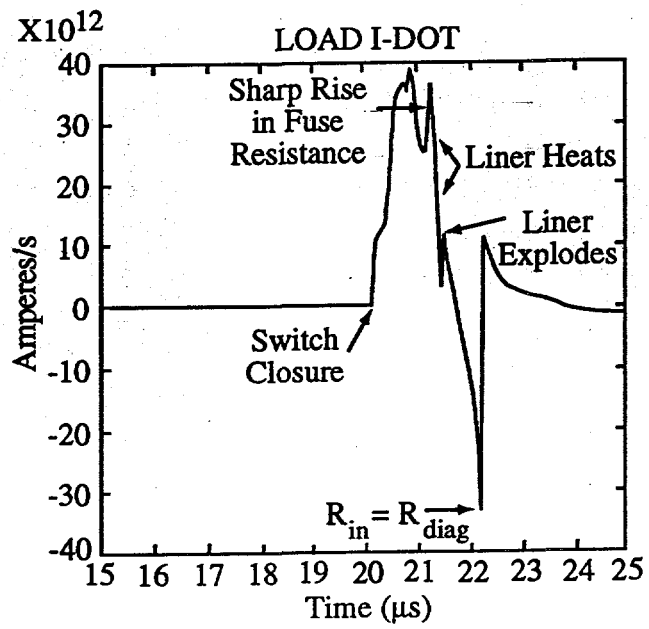


Figure 6c.

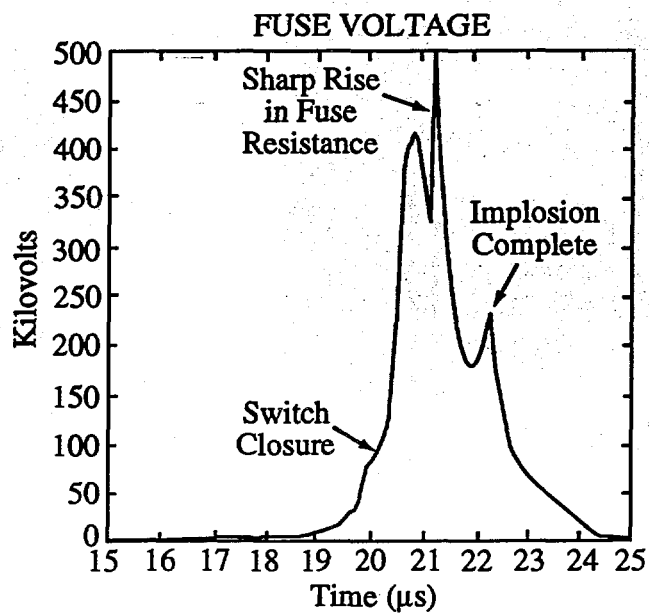
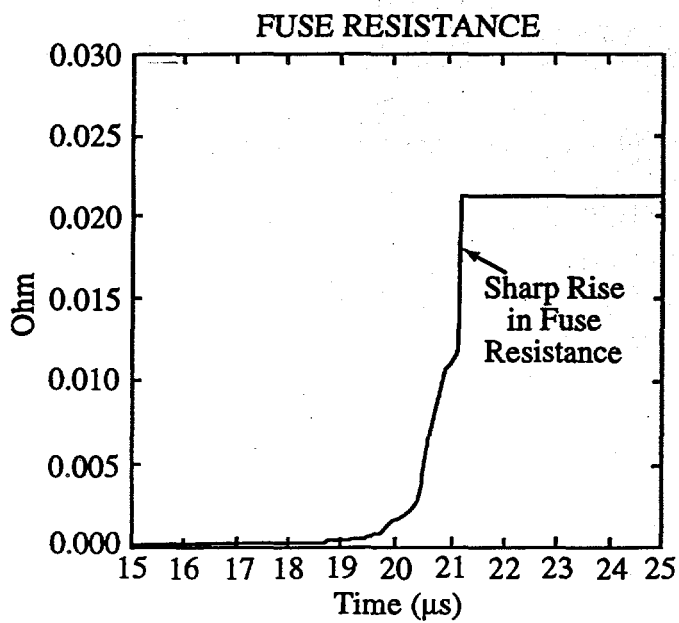


Figure 7.

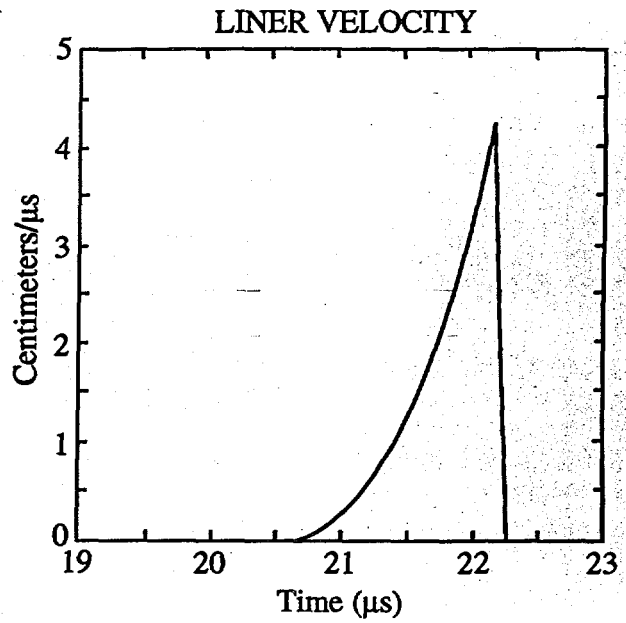
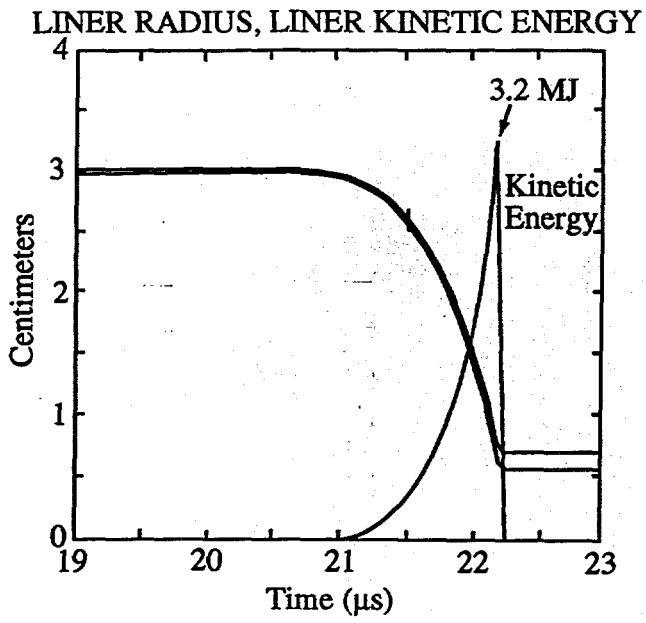


Figure 8.

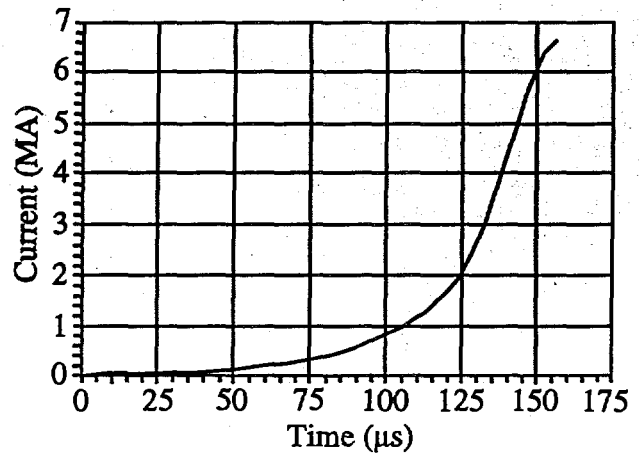
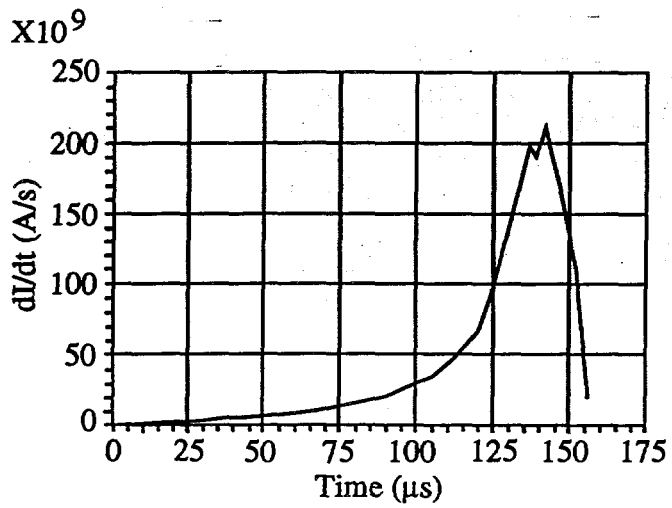


Figure 9

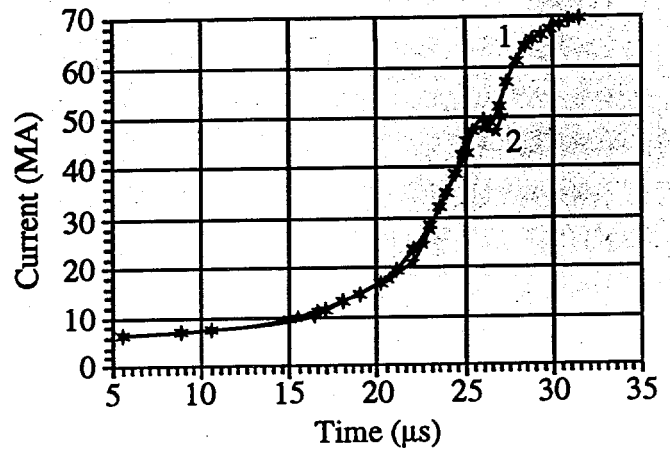
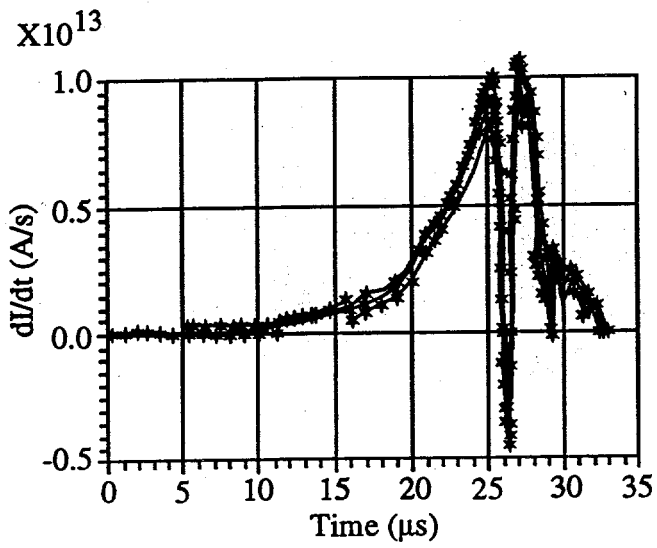


Figure 10.

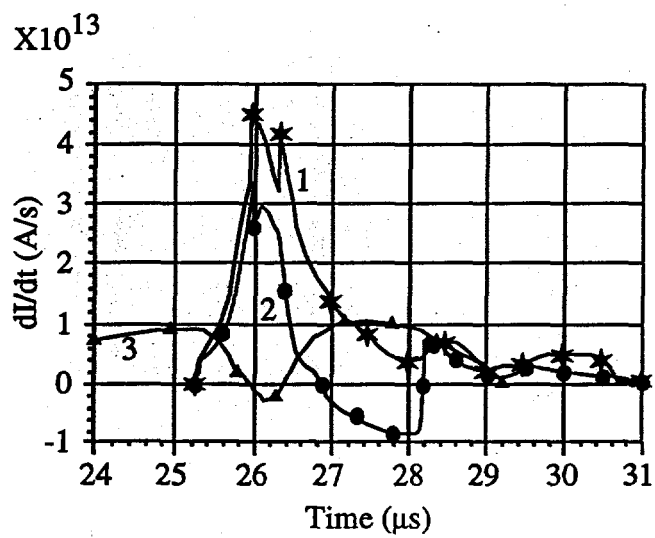


Figure 11.



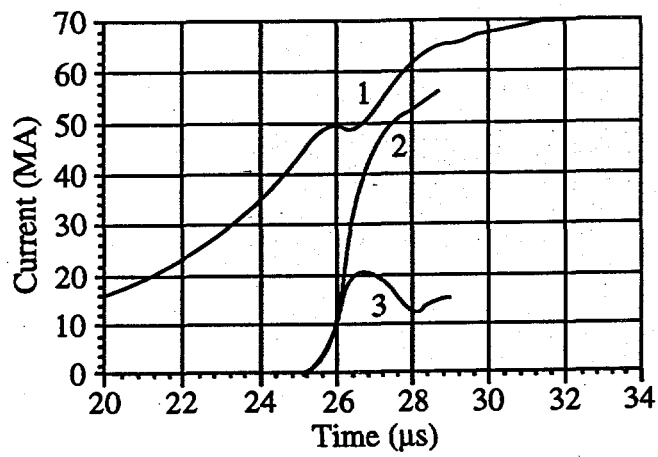


Figure 12.

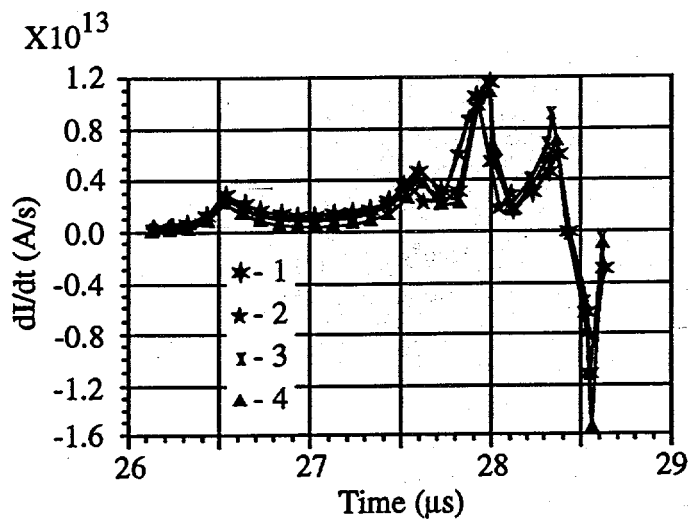


Figure 134

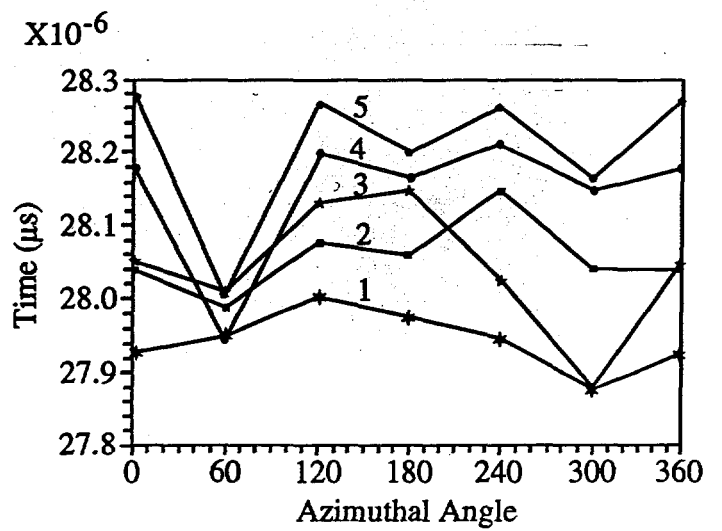
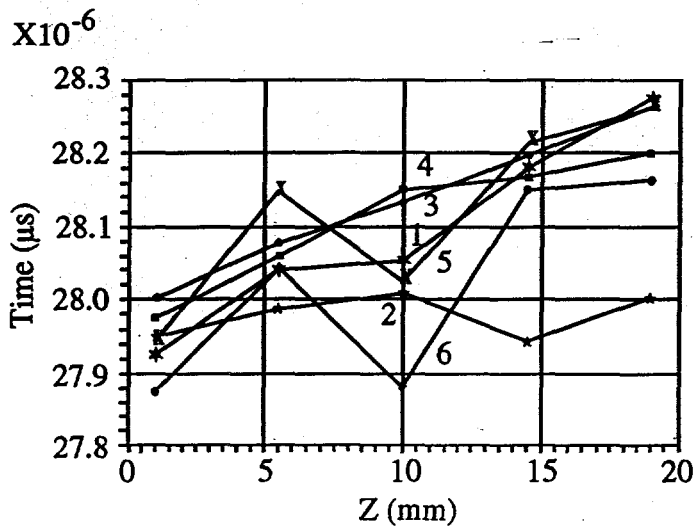


Figure 14.

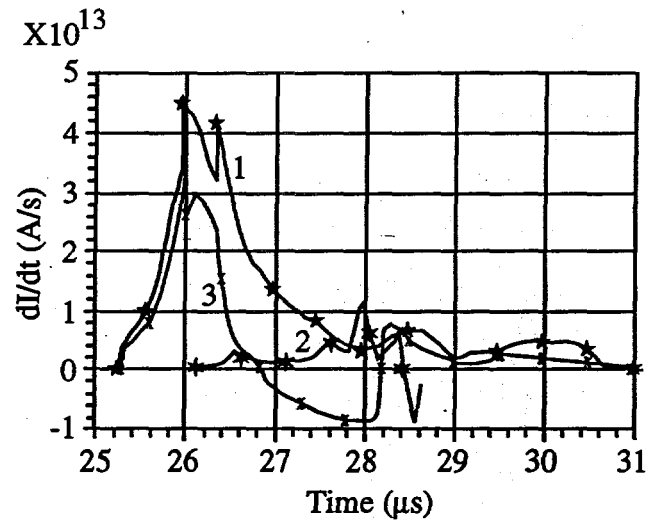


Figure 15.

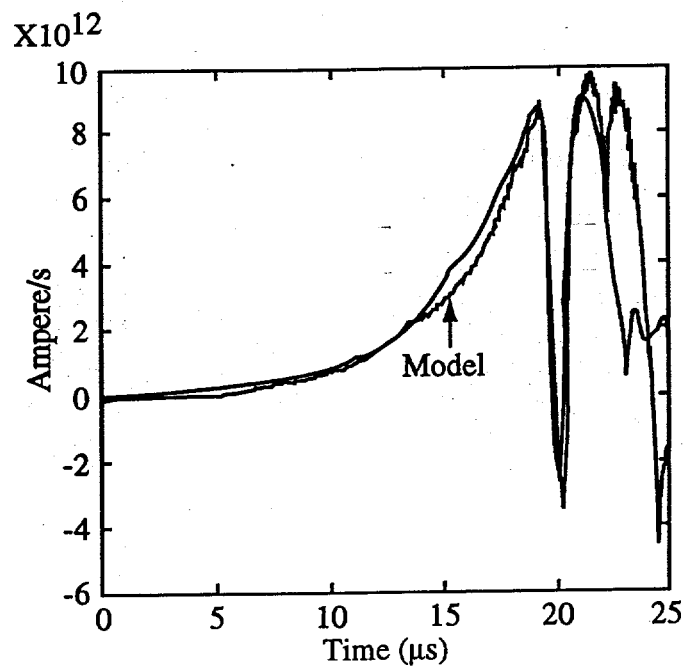


Figure 16.

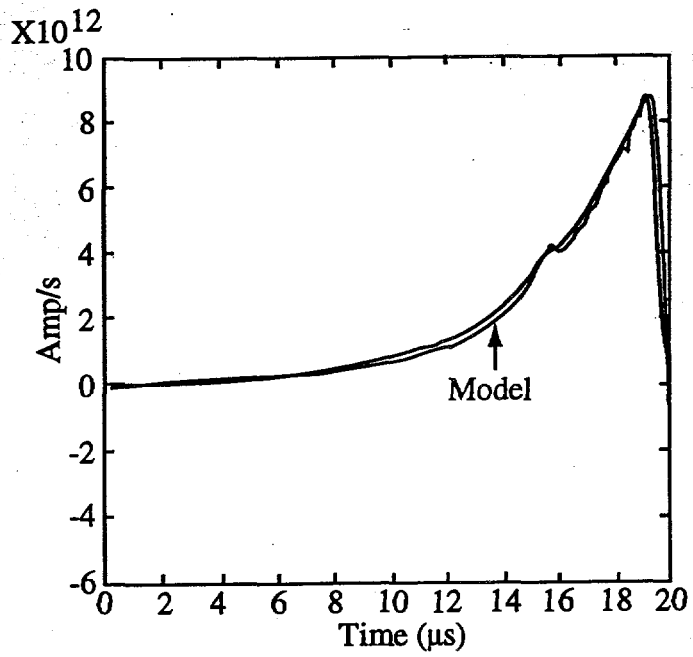


Figure 17.